ELSEVIER

Journal of Electron Spectroscopy and Related Phenomena 117–118 (2001) 71–88

JOURNAL OF ELECTRON SPECTROSCOPY and Related Phenomena

www.elsevier.nl/locate/elspec

Correlation effects and magnetism in 3d transition metals

Jürg Osterwalder*

Physik-Institut, Universität Zürich, Winterthurerstr. 190, CH-8057 Zürich, Switzerland

Abstract

Over the last few years the electronic structure of nickel metal has been investigated in quite some detail using high resolution photoemission spectroscopy. Important results from these studies are (i) that regions in momentum space could be identified where the exchange splitting for both d and sp bands could be measured directly in the vicinity of the Fermi level, and (ii) that these magnetic splittings continuously vanish as the Curie temperature T_c is approached. Spectral functions calculated using a multiorbital Hubbard model [Manghi et al., Phys. Rev. B, 59 (1999) R10409] provide an almost quantitative description of the data, marking the importance of spin- and momentum-dependent correlation effects on the energy scale of 100 meV. The behaviour of band magnetism in the vicinity of an interface is illustrated by discussing two adsorbate systems: hydrogen on Ni(110) and one monolayer of hexagonal boron nitride (h-BN) on Ni(111). There is evidence emerging that the bulk-like bands that are formed by the Ni atoms adjacent to the interface are strongly affected by the chemical bonding. In the photoemission data this results in a spectral weight transfer away from the bulk bands, in the formation of strong surface umklapp bands, and in slight energy and/or momentum shifts. For cobalt, the picture is not so complete, yet. A high-resolution Fermi surface map is presented for a thick Co film on Cu(111), and the relation to band structure calculations and correlation effects are discussed.

Keywords: Photoemission; Itinerant ferromagnetism; Electron correlation; Nickel; Cobalt; Surface electronic structure; Interface effects

1. Introduction

The itinerant ferromagnets Fe, Co and Ni and their alloys represent the most important base materials for low- and high-tech magnet applications. In addition to their large magnetic moments, it is the itineracy, i.e. the participation of the magnetic d electrons in the Fermi surface, that makes them strong and highly tuneable magnets. The very same feature, on the other hand, has made them the subject of a continuing intense study and controversial discussion since the early days of solid state physics [1].

The ground state of an itinerant ferromagnet is characterized by a bandstructure, in which the spin-degeneracy of simple metals has been lifted: single particle states described by the same wave vector $\vec{k}$ but different spin quantum numbers — antiparallel ($\uparrow$) or parallel ($\downarrow$) to a defined magnetization direction — have their energies separated by the exchange splitting $\Delta E_{\mathrm{ex.}}(\vec{k}) = \varepsilon^{\downarrow}(\vec{k}) - \varepsilon^{\uparrow}(\vec{k})$. Bringing the Fermi levels in the two spin-subbands to equal energy positions thus leads to a lopsided population, with more spin-up (hence majority) than spin-down (minority) electrons [2,3]. This model due to Stoner gives a qualitative description of the formation of local moments and their temperature behaviour up to the Curie temperature T_c, and it provides a simple so-called Stoner-criterion for when

*Tel.: +41-1-635-5827; fax: +41-1-635-5704.
E-mail address: osterwal@physik.unizh.ch (J. Osterwalder).

0368-2048/01/$ – see front matter
PII: S0368-2048(01)00246-8

a metal becomes unstable towards magnetic moment formation: $U \cdot D(\varepsilon_F) > 1$. Here, U is the average gain in Coulomb repulsion energy due to electron correlation and $D(\varepsilon_F)$ is the mean density of states at the Fermi energy per atom and spin-subband. This simple criterion works well to explain the occurrence of ferromagnetism within the 3d transition metal row [4].

The reason for continuing research into this subject is twofold: the Stoner model has failed to give more quantitative results on such properties as the magnetic moment and the value of T_c even when more and more sophisticated band structure theories were used. And, more importantly, local and non-local aspects of magnetic moment formation have been difficult to rationalize within one consistent theory: while there are no magnetic moments above T_c in the Stoner model, some experiments indicate their persistence in the paramagnetic phase: the Curie-law behaviour in magnetic susceptibility measurements, or the observation of spin waves above T_c by inelastic neutron scattering experiments [5].

The role of correlation effects in forming the ferromagnetic ground state is obvious: itinerant electrons of the same spin avoid each other due to the Pauli exclusion principle. The average Coulomb repulsion for parallel spin electron states is thus reduced and ferromagnetic spin alignment is favoured. The more localized the electronic states are, the more one approaches the limit of strong on-site correlation. In accordance with the Stoner criterion, the tendency for ferromagnetic order rises with U/W where W is the band width, since the density of states at the Fermi energy is roughly inversely proportional to the band width. The paramagnetic state results from thermal excitations of this ferromagnetic ground state. These excitations will be strongly influenced by electron correlation effects. The study of this excitation spectrum is therefore very interesting and may give experimental access to detailed parameters governing these collective phenomena.

2. Photoemission from itinerant ferromagnets

An obvious choice for investigating the detailed electronic structure and the excitation spectrum of an itinerant ferromagnet is high-resolution spin- and angle-resolved photoemission of the valence levels. In this experiment the spin-dependent hole spectral function $A_{\uparrow(\downarrow)}(\vec{k}, \varepsilon)$ can in principle be measured as a function of all parameters: spin, wave vector and energy [6]. The spectral function reflects the response of the interacting many-electron system to the removal of an electron of wave vector $\vec{k}$ and spin $\uparrow(\downarrow)$. Within the sudden approximation, the photoemission spectrum reflects this quantity, distorted by varying photoemission matrix elements and extrinsic inelastic scattering processes. Typically, the hole spectral function has some memory of the energy, momentum and spin of the removed electron and exhibits a well-defined so-called quasiparticle peak. Its line position is shifted from the bare single-particle energy towards the Fermi energy by an amount which equals the real part of the particle self energy. Its line width is given by the imaginary part of the particle self energy (see Section 3.2). Measuring these two quantities from a photoemission spectrum can thus provide experimental access to the self energy, and from comparison to model calculations to the manybody interaction parameters, such as the Coulomb repulsion integral U.

Two more quantities can be extracted from such quasiparticle peaks in a photoemission spectrum: intensity and spin polarization. Unfortunately, the measurement of spin is associated with a serious loss of sensitivity such that the energy and momentum resolution of the spectrometer have to be strongly relaxed [7]. Rather broad spectra with energy resolutions of typically 0.5 eV result, from which a detailed reconstruction of the band structure is not possible and the information on $A_{\uparrow(\downarrow)}(\vec{k}, \varepsilon)$ becomes rather limited [8–10]. An alternative approach has been to do high-resolution spectroscopy in a spin-integrated fashion [11–13]. In cases where exchange-split bands are well identified in the spectra, a comparison with single-particle band structure calculations proved reliable to identify the majority/minority character of measured quasiparticle bands.

The measurement of the quasiparticle momentum is complicated by the fact that photoemission conserves only the electron wave vector component $\vec{k}_{\parallel}$ parallel to the surface. The short probing depth and the propagation through the surface potential step broadens and reduces, respectively, the wave vector

component $k_\perp$ perpendicular to the surface. Photoemission calculations within the one-step model [14] considering appropriate time-reversed low-energy electron diffraction (LEED) states as photoelectron final states can overcome this problem quantitatively. However, such calculations are available only for few systems [15,16], and they have not yet been combined with the formalism of spectral functions. On the other hand, the much simpler three-step model [17] has proven quite successful when free-electron final states are used for describing the electron propagation through the solid to the surface (step 2) after the photoexcitation process (step 1) [6]. Transmission through the surface potential step (step 3), which is characterized by the inner potential V_0, can then be treated like a refraction at the boundary of two media: the plane wave outside the surface has a shorter $k_\perp$ than the one inside the solid. From the measured photoelectron kinetic energy in vacuum

$$E^m_{\mathrm{kin}} = h\nu - \Phi - E_{\mathrm{B}} \tag{1}$$

where $h\nu$, Φ and E_{B} are photon energy, work function and binding energy measured from the Fermi level, respectively, and from the emission polar angle θ_m (measured from the surface normal), one calculates readily

$$\left|\vec{k}_\parallel\right| = \frac{1}{\hbar}\sqrt{2mE^m_{\mathrm{kin}}}\sin\theta_m \tag{2}$$

and

$$k_\perp = \frac{1}{\hbar}\sqrt{2m(E^m_{\mathrm{kin}} + V_0)}\cos\theta \tag{3}$$

where

$$\sin\theta = \sin\theta_m\sqrt{\frac{E^m_{\mathrm{kin}}}{E^m_{\mathrm{kin}} + V_0}} \tag{4}$$

is the sine of the refracted polar angle. Within the free-electron final-state approximation these components define the $\vec{k}$-vector of the hole inside the solid for a particular sample azimuth ϕ. Matters become much simpler in two-dimensional systems such as surface states or ultrathin films, where only $\vec{k}_\parallel$ is relevant [18].

Unfortunately, also the measurement of the quasiparticle life time, which is related to the imaginary part of the self energy, is not straightforward [19,20]. The line widths in photoemission spectra contain contributions from the hole (=quasiparticle) life time and from the photoelectron life time. The latter is related to scattering processes in the final state and thus to the finite probing depth, and it is irrelevant for the analysis of electron correlation effects in or near the ground state of the solid. The two contributions to the line width add in a nontrivial way, depending via the particle group velocities on the detailed band structure and on the emission angles [19,20]. Here again, two-dimensional systems are free from these complications: due to the lack of dispersion along $k_\perp$ of the photohole, the photoelectron life time contribution is not seen in the spectrum [19,20].

In this review we emphasize two particular types of photoemission data sets that have proven to be particularly useful for studying the electronic structure of itinerant ferromagnets.

(i) Dispersion plots are generated by taking full photoemission spectra for a continuous series of polar or azimuthal angles. If the measured intensities are plotted as gray scale values in a binding energy versus angle diagram, bands dispersing along this particular $\vec{k}$-space section become apparent (see e.g. Fig. 2b–d). For each binding energy, the $\vec{k}$-vector moves along a circular line in reciprocal space (constant energy $E^m_{\mathrm{kin}} + V_0$ of the free-electron final state) with radius

$$k = \frac{1}{\hbar}\sqrt{2m(E^m_{\mathrm{kin}} + V_0)} \tag{5}$$

and with refraction effects according to Eq. (4). At the photon energies typically used for such studies, these $\vec{k}$-vectors lie in the second Brillouin zones of the periodic zone scheme for 3d transition metals. Whenever $\vec{k}$ moves across a band for this particular binding energy, i.e. when it meets the dispersion relation $\varepsilon(\vec{k})$, high photoemission intensity is measured [21].

(ii) Constant energy maps or, more specifically, Fermi surface maps result from taking photoemission intensities at just one binding energy and scanning both emission angles over most of the hemisphere above the surface [22]. The sampled $\vec{k}$-vectors then sweep the surface of a spherical sector of a radius as described by Eq. (5), and with its opening angle reduced by

refraction effects as compared to the polar angle range measured outside the crystal. Whenever $\vec{k}$ moves through a band at this particular binding energy, the photoemission intensity $I(\theta_m, \phi)$ rises.

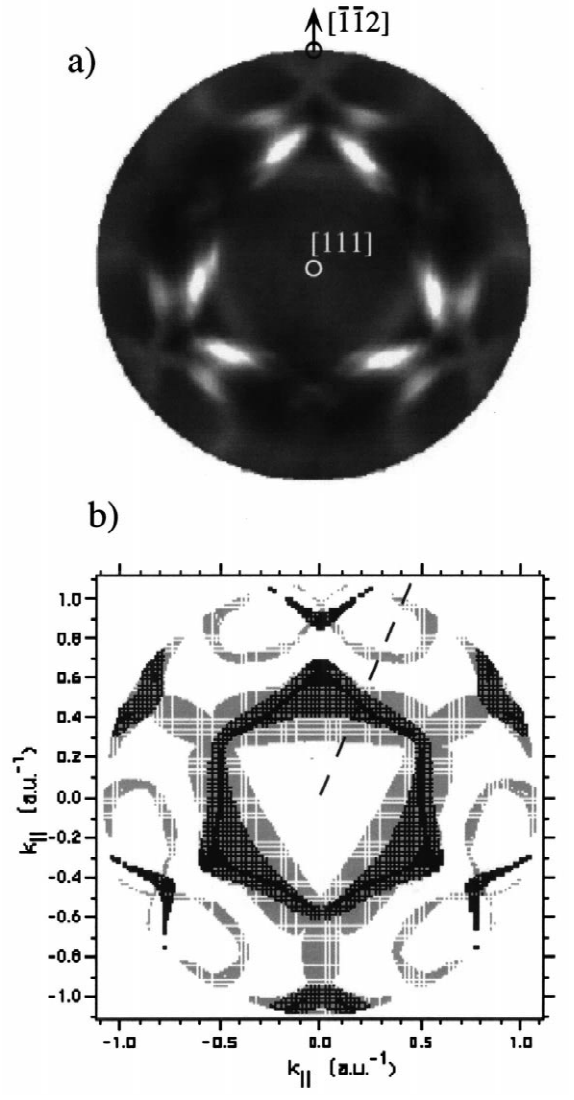

Fig. 1. (a) He Iα excited Fermi surface map ($h\nu = 21.21$ eV) from Ni(111). A $\vec{k}_{\parallel}$ projection of the raw data is presented in a linear grey scale, with highest intensities in white, lowest in black. In (b) the corresponding spin-polarized LKKR calculation (see text) is displayed, showing Fermi level crossings at the same $\vec{k}$ locations as in the measurement (a). Majority spin bands are shown in black, minority spin bands in grey. The dashed line indicates the polar scan along which the data of Fig. 2 have been measured (from Ref. [13]).

These locations form continuous contours on an $I(\vec{k}_{\parallel})$ grey scale plot (see e.g. Fig. 1a) because $\varepsilon(\vec{k})$ is a continuous function for each individual band. This pictorial representation of energy and momentum conservation in the photoemission process is illustrated comprehensively in Ref. [23].

All the data presented in this review have been measured in laboratory-based photoelectron spectrometers at the Universities of Zürich and Fribourg (Figs. 7 and 8) using monochromatized or non-monochromatized He I radiation. The angular scanning is done sequentially by means of a computer-controlled high-precision sample goniometer [24]. Dispersion plots typically contain 50 angular settings, Fermi surface maps about 4000. Measuring times range from 30 min up to a few hours, depending on the sampling density, the selected angle and energy resolution and the photoelectric cross sections. For the data presented in this work, the angular resolution has been set to about $\pm 1°$ and the energy resolution is of the order of 40 meV. This is not the highest resolution by today's standards, but it is well matched to the spectral features near the Fermi energy of 3d transition metals: the measured line widths are not limited by the instrumental resolution.

3. Nickel

Of the three ferromagnetic 3d transition elements, nickel has the smallest magnetic moment (0.6 μ_B, versus 1.7 μ_B and 2.2 μ_B for cobalt and iron, respectively). As a consequence, it is the most itinerant of all three, and it has led to stronger controversies than the other two. Earlier spin-polarized photoemission work reported both a collapse of exchange splitting at T_c and remaining split bands, depending on the particular region in momentum space that was probed [8–10]. It was argued that this property may depend on the group velocity of the respective bands: higher group velocity means that the electron states probe a larger area in real space and are thus more susceptible to magnetic fluctuations; the exchange splitting of these bands will thus progressively collapse as T_c is approached from

below. More localized, low group velocity states, on the other hand, feel the local exchange correlation potential and are less affected by magnetic fluctuations [25]. However, this view did not withstand careful scrutiny by high-resolution photoemission experiments [12].

3.1. Low-temperature electronic structure

While many of the earlier spin-polarized experiments were probing bands at considerable distance away from the Fermi energy, high-resolution experiments revealed well developed exchange splittings at room temperature in the vicinity of ε_F for both low group velocity d states and high group velocity sp states alike [11]. For the elucidation of how the magnetic and electronic properties are related, such $\vec{k}$ locations are the most interesting ones because this is where the occupation numbers for majority and minority spin bands are determined. The finding of such locations is strongly facilitated by recording Fermi surface maps. In Fig. 1a, one such data set, measured at room temperature on a Ni(111) surface at a photon energy of 21.21 eV, is shown (from Ref. [13]). Well defined Fermi surface contours show the threefold rotational symmetry of the face-centered cubic lattice viewed along the [111] direction. In order to identify the specific spin and angular momentum character of the states that produce these Fermi level crossings, we give in Fig. 1b the result of a spin-polarized layer-Korringa-Kohn-Rostocker (LKKR) band structure calculation carried out for exactly the same wave vectors. All calculated Fermi surface contours are also seen in the experimental data set, although somewhat intensity modulated by matrix-element effects. Evidently, there are contours that have clearly minority (↓, grey) character, at some places both spin polarizations appear superposed upon each other, and in some regions there are fine splittings that should be particularly suitable to study magnetic effects.

In order to establish the sp- or d-type nature of the observed states, it is useful to study the energy dispersion of the various bands. The Fermi surface map of Fig. 1 may serve as a convenient guide for along which directions these dispersion plots should be taken. The particular polar angle scan shown in Fig. 2b [12], which follows the dotted line indicated in Fig. 1b, reveals the dispersing bands responsible for the two dominant bright features in each irreducible 60° sector of the Fermi surface map of Fig. 1a. The upside-down parabolic shape of this band tells us that we are dealing with the top of the minority d band. At least we observe a d-band maximum with respect to one of the three directions in three-dimensional $\vec{k}$ space, and band structure calculations indicate that dispersion is weaker along the other two directions. Roughly 300 meV below the minority d-band parabola there is the corresponding majority band, following the same parabolic shape. It should

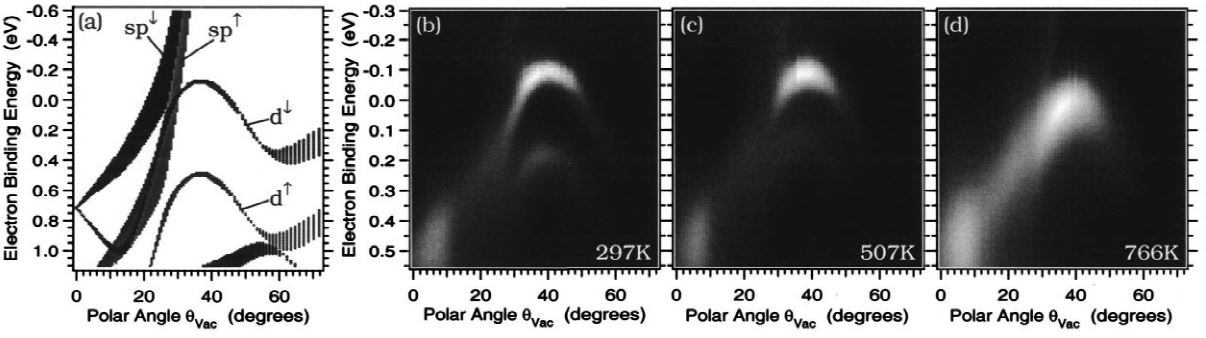

Fig. 2. (a) Spin-polarized LKKR calculation for band dispersion in the $\vec{k}$ space region defined by the dashed line in Fig. 1b. Note that majority spin bands are now given in grey, minority bands in black. The bands are labeled according to their dominant angular momentum character. (b–d) He Iα excited ($h\nu = 21.21$ eV) polar angle scans of photoemission spectra along the same $\vec{k}$ space region of Ni(111), which is in the azimuth 23° off the [-1-12] direction, measured at three different temperatures: (b) 0.47 T_c, (c) 0.80 T_c and (d) 1.21 T_c. The intensities are presented in a linear grey scale with maximum intensity in white. All spectra have been normalized by a Fermi–Dirac distribution function in order to remove occupation numbers from the measured bands (from Ref. [12]).

be noted that the minority band clearly crosses the Fermi level and reaches up to an energy of about 100 meV above ε_F. The dispersion has in this region been made visible by normalizing measured intensities by thermal occupation numbers, i.e. by dividing intensities by the Fermi–Dirac distribution function [12]. We have thus identified a magnetically active region in k-space where occupation numbers are strongly spin dependent.

Again it is instructive to compare these measured bands to the result of a band structure calculation, which is given in Fig. 2a for the same section through $\vec{k}$-space. One finds a rather good qualitative agreement of the band dispersion, with both d-band parabola also present in the calculations and with the minority d-band crossing the Fermi level at roughly the same angles (i.e. the same $\vec{k}$-vectors). In addition, the fast dispersing sp-bands appear in the calculations, also crossing ε_F very close to a d-band crossing. Upon closer inspection, the sp-bands can also be found in the experimental data, appearing as a faintly bright trace just at the left side of the minority d-band parabola. Such calculations thus reproduce these high-resolution data in essentially every detail.

However, there remain strong systematic deviations from experiment in the calculated binding energies: in order to make the apparent dispersions match in Fig. 2a and b, the energy scale for the calculated bands has to be compressed by roughly a factor of 2.5. This kind of energy renormalization is now well understood: it is a consequence of electron correlation effects.

3.2. Correlation effects

Within the sudden approximation description of the photocurrent, the measured spectrum reflects the hole spectral function $A_{\uparrow(\downarrow)}(\vec{k}, \varepsilon)$, weighted by matrix elements and extrinsic inelastic scattering effects, and with uncertainties in $\vec{k}$ as discussed in Section 2. In the case of non-interacting particles, such as inherently generated in a band structure calculation carried out within the local density approximation (LDA), $A_{\uparrow(\downarrow)}(\vec{k}, \varepsilon)$ consists of a set of delta functions $\delta(\varepsilon - \varepsilon_i(k))$, one placed at the eigenvalue $\varepsilon_i(k)$ of each band i for a given wave vector $\vec{k}$. For interacting electrons, the spectral function reflects the full manybody response of the solid surface to the removal of one particle. The remaining hole strongly couples to the charges and spins of the other electrons, and to other excitations such as e.g. phonons (see below). This dressed hole — or quasiparticle excitation — has associated with it a self-energy $\Sigma_{\uparrow(\downarrow)}(\vec{k}, \varepsilon)$ which accounts for all these manybody effects. The real part of Σ reflects the manybody correction to the single-particle energy, which can be viewed as the energy gain of the system due to the screening of the photohole. This energy gain is carried away by the photoelectron which thus appears shifted to higher kinetic energies by the amount of $Re(\Sigma)$. These same screening effects contribute to the lifetime of the hole, which is thus inversely proportional to $Im(\Sigma)$. In addition, the spectral function usually contains an incoherent part, consisting of a broad spectrum at higher excitation energies, i.e. lower photoelectron energies. In this part of $A_{\uparrow(\downarrow)}(\vec{k}, \varepsilon)$ the memory of the energy and momentum of the photohole have been lost.

In the case of itinerant ferromagnets, the self-energy and thus the spectral function depend on the spin of the photoexcited electron. The situations for majority and minority spin photoemission are depicted in Fig. 3. All the electronic manybody responses of the solid to the creation of the photohole

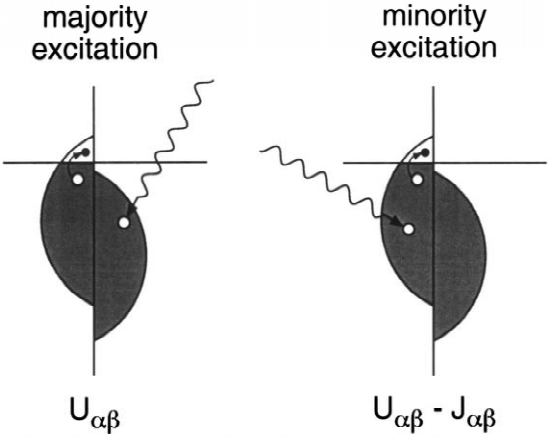

Fig. 3. Schematic representation of the interactions involved in the photoemission from majority and minority spin bands. The resulting interaction strengths are given below the figures (see text; from Ref. [26]).

involve the formation of electron–hole pairs of single particle states, which can only occur with high efficiency in the minority channel due to the high d-electron density of states. For majority spin photoemission (Fig. 3a) these extra holes and the photohole have different spins. The full phase space is thus available for the manybody response and self-energy effects can be large. For minority spin photoemission, the situation is complicated by the exclusion principle for the two holes, and the number of scattering processes is thus reduced. We therefore expect such manybody effects to be weaker for minority than for majority spin photoemission. Qualitatively, we should see thus a strong shift of majority bands towards ε_F and a smaller shift of minority bands. As a consequence the measured exchange splitting is substantially smaller than the one obtained within a single particle picture. In Fig. 2 we saw that these effects reduce ΔE_{ex} by roughly a factor of 2.5.

Recently, Manghi et al. [26] have adopted a three-particle approximation to the full electronic many-body problem in order to treat these effects numerically. The photohole and one single electron–hole pair are considered and made to interact in a Hubbard model. The starting point for these so-called 'three-body scattering' (3BS) calculations is a band structure calculation. The resulting eigenvectors serve to decompose for each vector $\vec{k}$ the corresponding eigenstates into sp-like or d-like contributions. The Coulomb integral U in the 3BS Hubbard model intervenes only for the d-contribution which is highly localized. The numerical solution of this model results in momentum- and spin-dependent self-energies. Both lifetime broadening and energy shifts away from the single particle bands thus depend on momentum and spin. This is illustrated in Fig. 4 for a polar scan of spectra near ε_F measured on Ni(110). The raw data are shown in Fig. 4a, while the single-particle bands, calculated for the same

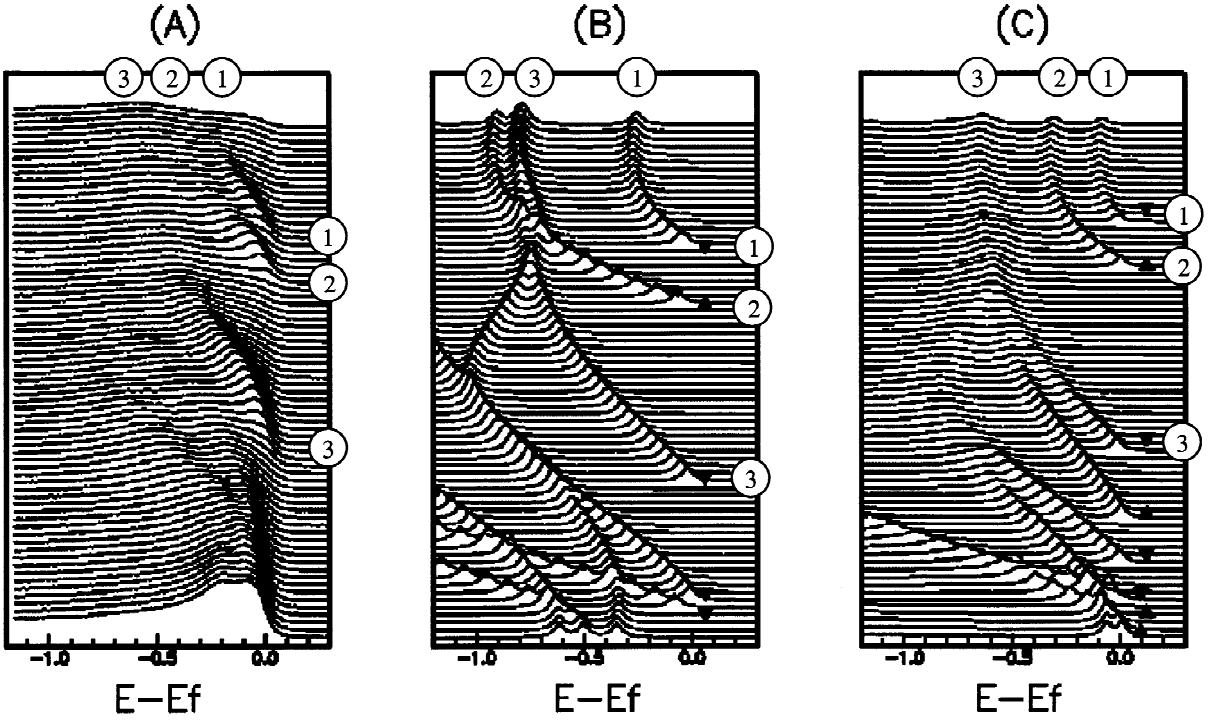

Fig. 4. Comparison between experimental photoemission data near the Fermi energy from Ni(110) (a), single particle local-density approximation (LDA) calculations (b), and quasiparticle 3BS results (c) (see text). The data span polar angles from 0° (bottom) to 70° (top) in 1°-steps within the (001) plane of nickel. The spin character is indicated by ▲ (majority) and ▼ (minority), and three bands are labeled for discussion (from Ref. [26]).

region in $\vec{k}$ space, are given in Fig. 4b. As observed also on Ni(111) (Fig. 2), the LDA calculations produce bands all the way down to binding energies of 1 eV and higher. Here, the delta functions have been convoluted with Lorentzians that correspond to the instrumental resolution of 40 meV. In the 3BS quasiparticle calculations [26], the situation has dramatically improved. All bands essentially disappear slightly below 0.5 eV binding energy, either because of excessive broadening associated with the imaginary part of the self-energies, or because they have shifted closer to ε_F. There is one exception to this behaviour: one single band near the bottom of Fig. 4c which disperses fast and is thus essentially sp-like. It is not clear why it is not seen in the experimental data. As far as energy positions of quasiparticle bands are concerned, there is now an almost quantitative agreement with the experimental data. This is more clearly seen in individual spectra, such as shown in Fig. 5 for three arbitrarily chosen emission angles. The upper three panels show once more how the LDA bands (lines) fail to reproduce the measured spectra (dots). In the lower panels, the 3BS quasiparticle peaks give a fair description of the data. Remaining inaccuracies are of the order of 150 meV or less. The strong spin-dependence of the self energy effects is evident e.g. in the two bands labeled (2) and (3) in Fig. 4: according to the spin-polarized LKKR calculation, band (2) has majority and band (3) minority character. In the single particle calculation (Fig. 4b) the two bands cross each other. At binding energies higher than the crossing point, both of them exhibit a low group velocity along this $\vec{k}$ direction. Upon turning on the three-particle interactions (Fig. 4c) the majority band (2) is shifted much closer towards ε_F, and the two bands no longer intersect. Majority spin excitations are thus much more strongly affected.

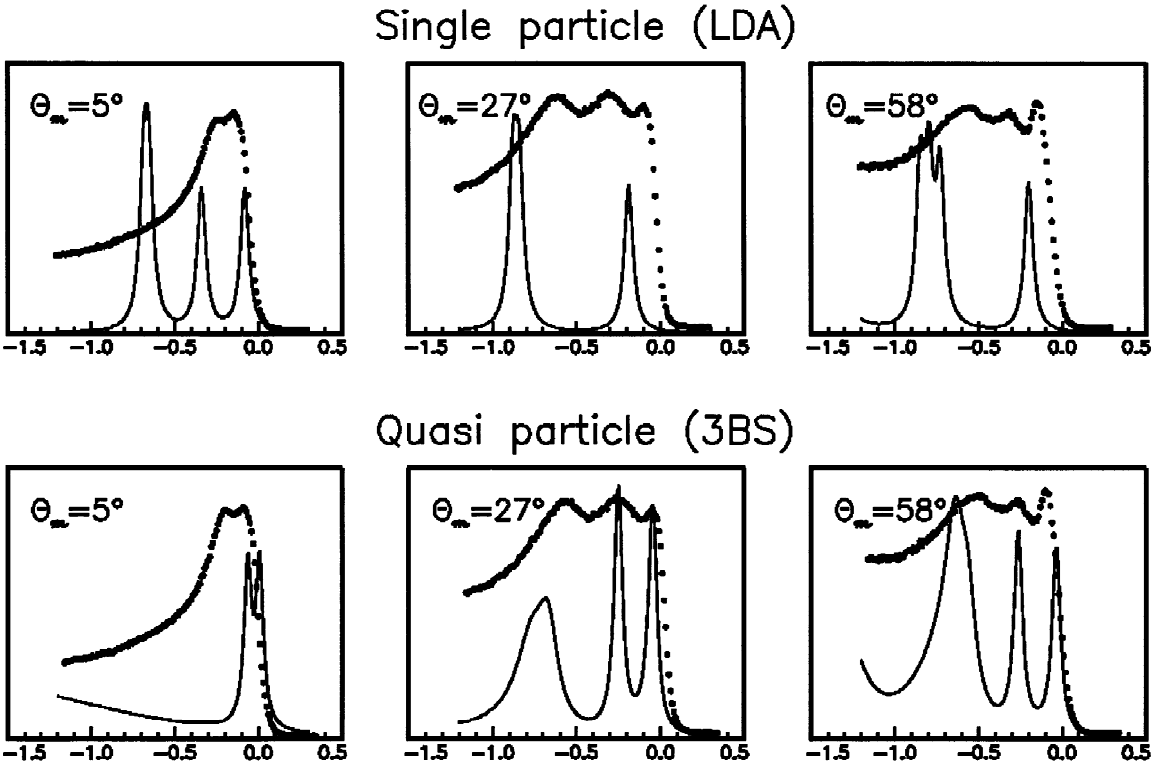

Fig. 5. Comparison between $\vec{k}$-resolved photoemission spectra (dots) extracted from Fig. 4a and theoretical spectral functions (continuous lines) calculated according to single-particle LDA (top) and quasiparticle 3BS (bottom) approaches. The $\vec{k}$ points correspond to the labeled values of the polar angle θ_m and to energies taken near ε_F (from Ref. [26]).

It may be pointed out that also the Fermi level crossings, i.e. the Fermi surface contours are slightly shifted by these correlation effects. The LDA calculations give a fair description of measured contours, but the quasiparticle calculations move the contours by up to 5° in polar angle to give an even better agreement with the data [26]. This is not defying the Luttinger theorem [27] because manybody interactions can distort a Fermi surface while keeping its volume conserved, and in a multiband system like Ni even particle transfer from one band to the other is conceivable.

Again looking at Fig. 5 we note that the line widths are, in contrast to the line positions, not well reproduced by the 3BS calculations. As mentioned before, the measured line widths are not limited by the instrumental resolution which was 40 meV. There are several reasons for these remaining discrepancies: the first has to do with the mixing in of the photoelectron lifetime in photoemission experiments from three-dimensional systems [19,20], as discussed in Section 2. A second reason may lie in the 3BS scattering approach: considering only single electron–hole pairs may be a reasonable truncation for the calculation of the real part of Σ but less so for the imaginary part. Last but not least we should not forget that this quasiparticle picture considers only the self-energy due to electron–electron interactions Σ_{e-e}, while other interactions such as electron–phonon (Σ_{e-p}) or electron–impurity (Σ_{e-i}) scattering may be important as well. Moreover, electron–magnon interaction (Σ_{e-m}), which has only been considered for Ni using a highly simplified band structure [28,29], may be important in this ferromagnetic system.

3.3. The magnetic phase transition

Nickel has a Curie temperature T_c of 631 K, which is easily reached in a high-resolution angle-resolved photoemission experiment. However, for the high-temperature measurements shown in Fig. 2c and d [12], precautions had to be taken in order to avoid deviations of photoelectron momenta due to the heater magnetic fields. Pulsed AC heating with electron counting gated off during the heater pulses [30] proved to give stable, unperturbed high-temperature spectra. The collapse of the exchange splitting of the d-band is seen clearly. Spin-dependent occupation numbers change strongly with temperature, reaching equilibrium with equal majority and minority numbers at T_c. From this observation the obvious conclusion is that there is no magnetic moment left in Ni at T_c.

How can this strong statement be reconciled with the findings of other experimental techniques that there are magnetic moments present as fluctuations above T_c, e.g. in the form of spin wave excitations [5]? One may get a hint from looking more closely at the spectra that constitute the data of Fig. 2. In Fig. 6 extracted spectra are given, normalized by thermal occupation numbers to show peaks also above ε_F [12]. The selected set of spectra is taken at the apex of the parabolic d-band. The two tops of the d-bands converge to meet exactly at the Fermi energy, even though their low-temperature starting points are asymmetric (180 meV and −100 meV binding energy, respectively). At this particular point in k-space it therefore costs no energy to flip a spin and thus to create a local moment as a fluctuation. Because this happens just at the apex, the density of

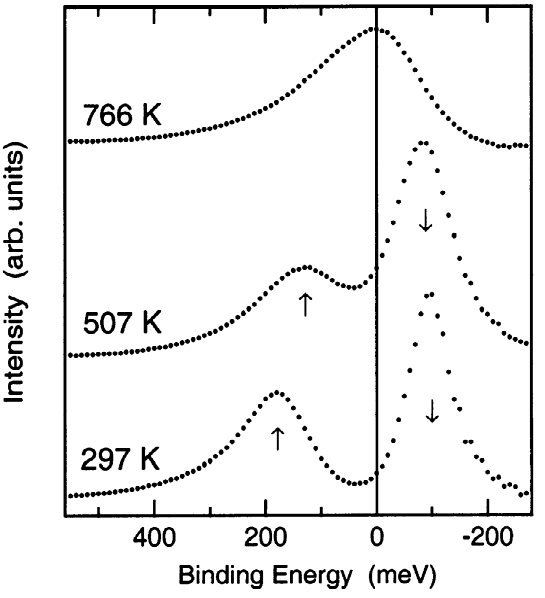

Fig. 6. Energy distribution curves from Ni(111) at three different temperatures, extracted from the Fermi–Dirac normalized data of Fig. 2b–d at the apex of the d bands ($\theta_m = 40°$). Spin labels are indicated by the arrows. The curves are drawn with intensity offsets (from Ref. [12]).

states available for such fluctuations is large, and more measurements at different locations on the Fermi surface suggest that the phase space where the d-band apex touches ε_F is quite large. It would, of course, be important to use tuneable synchrotron radiation in order to determine if this situation is globally true and the d-band maximum lies at ε_F throughout $\vec{k}$-space. A further indication for this fluctuation picture is that the d-band peak is anomalously large above T_c; it is significantly larger than the coalesced sp-band peaks measured above T_c [21] (see e.g. Fig. 7a). Each fluctuation will couple to a bath of spin waves, and depending on the wave number of the spin wave, the local band structure will show some degree of exchange splitting. The momentum average of all these spin-wave excitations may lead to this substantial broadening.

The exchange splitting in the sp-like band collapses concurrently with that of the d-band. This is most clearly illustrated in Fig. 7a where angular distribution curves are given [21], i.e. linear sections through a Fermi surface map. Such data sets have more recently been termed momentum distribution curves [31]. The room temperature curve has been extracted from the data shown already in Fig. 4a. The doublet peak near $\theta_m = 50°$ corresponds to Fermi level crossings of sp-like bands near the Σ line in the three-dimensional Brillouin zone. Upon raising the temperature to nearly T_c, the two peaks coalesce to form a single peak of roughly equal width. In Fig. 7b it is shown how such data sets (Fig. 4a) can be used to extract very accurate dispersion curves of such high group velocity states. For each binding energy, the corresponding angular distribution curve is analyzed by a curve-fitting procedure using simple Lorentzian line shapes (Fig. 7b). A compilation of all

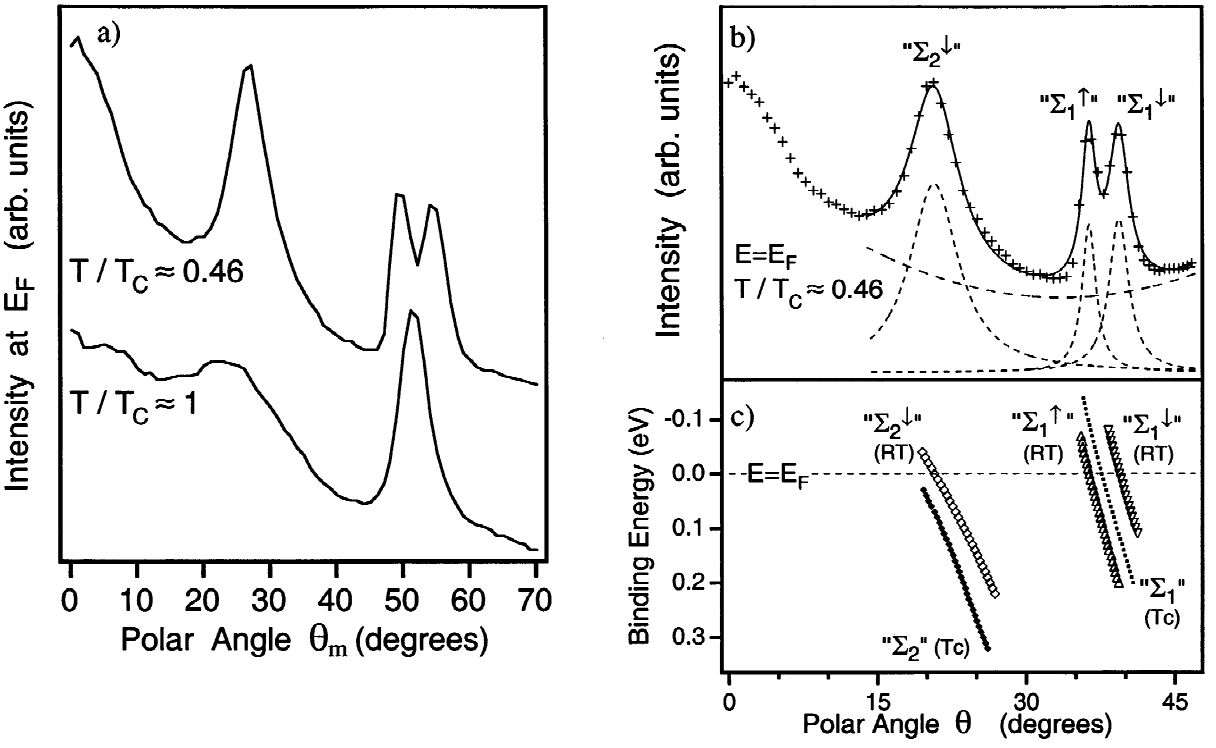

Fig. 7. (a) Polar intensity scans at the Fermi energy from Ni(110). The upper curve has been measured at room temperature (RT) and is from the data set already presented in Fig. 4a while the lower curve presents the measurement close to the Curie temperature. (b) Fitting of the RT data set (crosses) with Lorentzians (dashed lines) and a parabolic background leads to an excellent fit of the data (solid line). The peaks are labeled according to the symmetry line in $\vec{k}$ space close to which they appear. (c) Compilation of peak positions in angular intensity curves for a whole range of binding energies, both for RT data (open symbols) and T_c data (filled symbols) (from Ref. [21]).

the angular positions as a function of binding energy yields the highly accurate curves shown in Fig. 7c. In the room temperature dispersion curves the exchange splitting across ε_F can be evaluated as 204 +8 meV. It collapses to zero at T_c. In the same figure the minority d-like '$\Sigma_2^{\downarrow}$' state is seen pulled down by about 70 meV at T_c. From a fairly extensive set of similar data from two different Ni surfaces [11–13,21] the general picture emerges that in the vicinity of ε_F all spin-split states coalesce at T_c in a Stoner-like fashion. Earlier data suggesting some splittings remaining at T_c for features further away from ε_F need to be reevaluated.

3.4. Interface effects

All the observed bands discussed so far are considered to be true bulk states. This is corroborated not least by the excellent agreement between the spectra and the genuine bulk calculations in every detail. There have also been surface states reported near ε_F on Ni(111) [32,33] near the $\bar{\Gamma}$ point, but they are not visible at a photon energy of 21.21 eV. One may now wonder how the magnetic bulk states interact with the surface or more generally with interfaces, because it is well known that in the proximity of an interface the magnetic moments may change [25]. The question is whether photoemission at these energies can discriminate such interface effects. We expect to see the average band structure within the probing depth, which is only a few angstroms.

As a first example we consider an ordered adsorbate structure on Ni(110) formed by low-temperature exposure to hydrogen. The Ni atoms in the surface layer form a (2×1) pairing-row reconstruction with hydrogen atoms sitting in the two different threefold hollow sites located along the adjacent Ni rows [34]. Boschung et al. [35] have measured angle-resolved photoemission data at 150 K, scanning the same azimuth of the Ni(110) surface as were the data of Fig. 4a. Fig. 8 gives a summary of their data for the clean and hydrogen covered surface: (a) shows the whole sequence of spectra (as in Fig. 4) while (b) shows the same data in a linear grey scale in order to emphasize connected features. The clean surface data are very similar to the ones of Fig. 4, but the peaks near ε_F show up somewhat sharper due to the

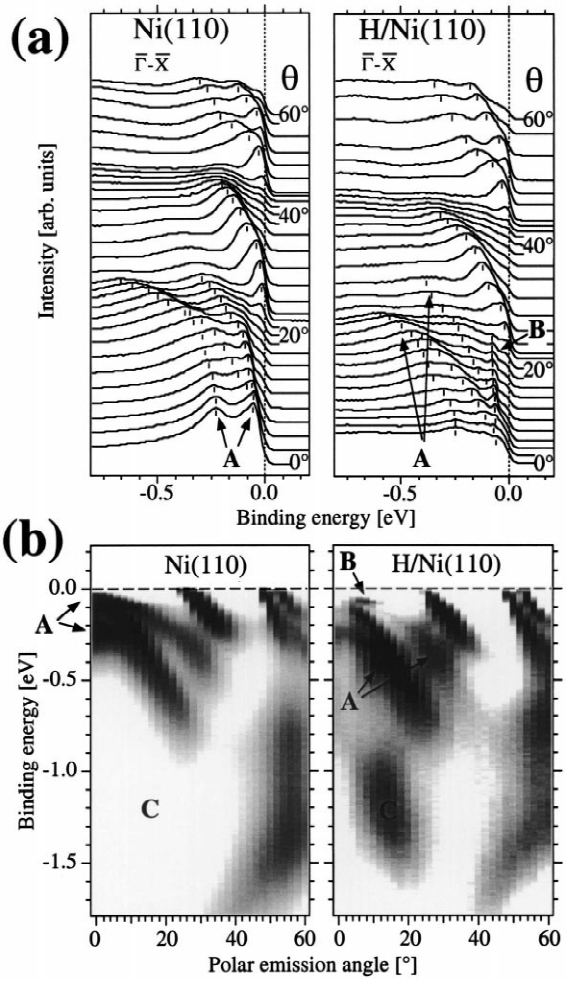

Fig. 8. (a) He Iα excited photoemission spectra ($h\nu = 21.21$ eV) near ε_F for the same $\vec{k}$ space scan as for the data of Fig. 4a from clean (left) and hydrogen saturated (right) Ni(110) at 150 K. (b) The same spectra in a linear grey scale (high intensities in black) dispersion plot down to 1.8 eV binding energy. Different features are labeled (see text; from Ref. [35]).

reduced temperature (150 K vs. 300 K). Upon hydrogen adsorption, two things happen: (i) there is a pronounced shift of spectral weight away from near ε_F to higher binding energies. This can be well understood by the hybridization of Ni 3d states from the top Ni layer with H orbitals, forming bonding and antibonding states [35]. Some of the bonding states may be found in the feature 'C' centered around 1.2 eV binding energy on the hydrogen covered sample. This apparent shift of spectral

weight without complete disappearance of the clean surface features is most simply explained by the finite probing depth of photoemission. Bands probed in the surface Ni layer have formed these hybrids and they no longer contribute to the spectral weight of the bulk-like bands, while these are still visible in the spectra from the probing of the subsurface region. (ii) Upon closer inspection one finds also slight shifts of the bulk bands upon hydrogen adsorption. However, one has to be careful in interpreting such shifts. The hydrogen adsorbate changes the work function of the surface from 4.7 to 5.3 eV. According to Eq. (1) the kinetic energy of the photoelectrons in vacuum $E^m_{\rm kin}$ is reduced by 0.6 eV, and slightly different $\vec{k}$-vectors (Eqs. (2)–(4)) are thus sampled at equal polar angles θ. Note that the inner potential V_0 is referenced to the vacuum level and that we assume that it is changed by the presence of the adsorbate by the same amount as the work function Φ, reflecting the fact that V_0 determines the strength of the refraction at the surface potential step. In this approximation the reduced work function produces a slightly weaker refraction but does not change the length of the internal $\vec{k}$-vectors. Nevertheless, in comparing spectra taken at equal polar angles θ, any dispersion along these momentum differences will show up as slight shifts in the spectra. Another contribution to such shifts may come from the surface reconstruction of the topmost Ni layer, shifting the corresponding surface d-states by small amounts due to the reduced atomic coordination and the different electron density due to the presence of hydrogen adsorbates. Again, photoemission should probe these surface d-levels as well as the underlying bulk bands. From Fig. 8a one gets indeed the impression that the hydrogen-covered sample produces generally broader spectra, corroborating this picture of a 'stratified' d-type band structure.

In more traditional language, such surface bands are termed either surface states or surface resonances, depending on whether their $\vec{k}_\parallel$ lies in a band gap of the surface-projected bulk band structure or not. In the case of Ni we are maybe dealing with a special case. There is an sp-like surface state on Ni(111), centered at Γ and closely related to the Shockley states on the noble-metal (111) surfaces [33]. A d-like Tamm state has been reported, also on Ni(111), with a binding energy of 0.25 eV at Γ [32]. However, also the surface Ni atoms have of the order of 9.5 d-electrons per atom which, due to their local character must contribute to the d spectral weight measured in photoemission. As is well known from tight-binding calculations, band structure has actually a fairly local aspect to it such that it is quite reasonable to think in terms of a surface-layer d-band structure.

In this new light it is actually surprising that we do not see more deviations in the measured spectra from the theoretical bulk calculations (Fig. 4). There may be two reasons for this: the very presence of the surface, together with the photoelectron inelastic mean free path, is responsible for a considerable uncertainty and broadening in $k_\perp$ and one may just not resolve these surface shifts. Secondly, there may be a subtle compensation effect on these shifts due to the correlation effects of the type described in Section 3.2. Clearly, the phase space for electron–hole pair creation is different at the surface due to dimensionality effects, and the self-energy related shifts may thus not be the same as in the bulk.

A nice illustration of this concept was found in a recent study of monolayer films of hexagonal boron nitride (h-BN) on Ni(111) [36]. Such films can be prepared in a highly perfect quality [37]; they form a fully commensurate, slightly corrugated graphite-like layer of (1×1) symmetry, with N atoms taking on-top positions above surface Ni atoms and B occupying fcc threefold hollow sites [38,39]. Fig. 9 gives two Fermi surface maps, one for the clean Ni(111) surface (Fig. 9a) and one for the h-BN covered surface (Fig. 9b). The work function drops from 5.4 eV for Ni(111) to a rather low 3.6 eV for the adsorbate-covered surface. In order to compensate for this significant difference, the two Fermi surface maps have been scaled properly in $\vec{k}_\parallel$ to account for the different refraction at the surface potential step (see discussion above). Within the free-electron final-state approximation, and with the assumption that the inner potential V_0 is reduced by the same amount as the work function, the two data sets displayed in Fig. 9 sample the same $\vec{k}$-vectors inside the solid, and any differences should reflect the changes in the electronic structure due to the presence of the h-BN monolayer. The most striking difference is a change from a threefold symmetric contour pattern to one with a predominant sixfold

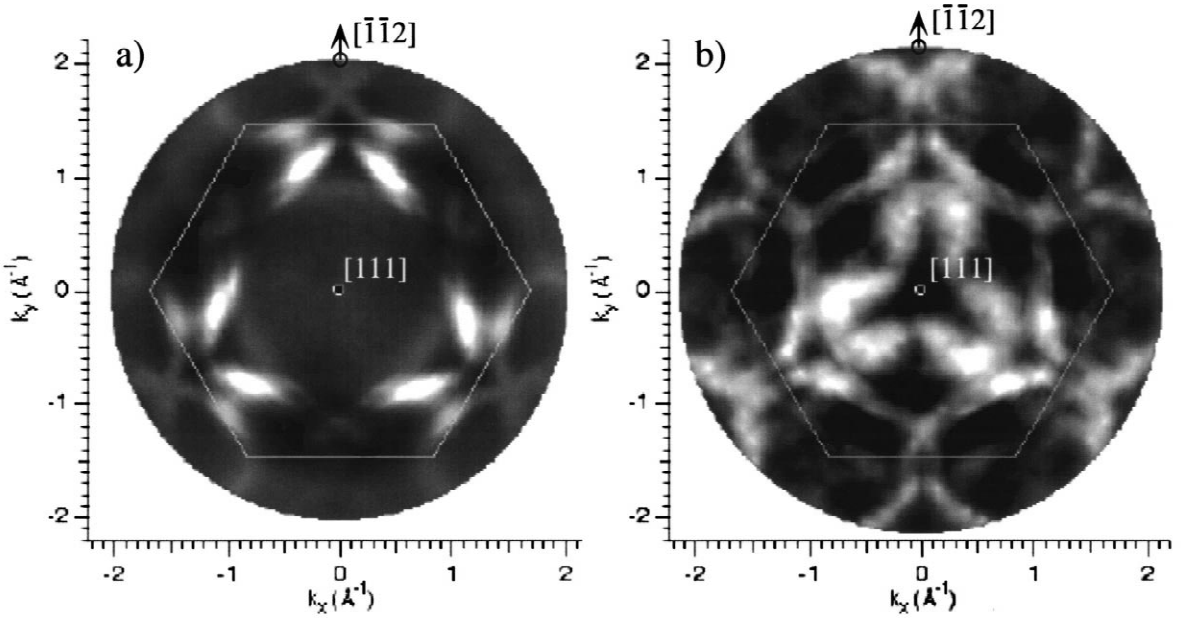

Fig. 9. (a) He Iα excited Fermi surface map ($h\nu$ = 21.21 eV) from Ni(111) (cf. also Fig. 1a). A $\vec{k}_{\parallel}$ projection of the raw data is presented in a linear grey scale, with highest intensities in white, lowest in black. (b) He Iα excited Fermi surface map from Ni(111) covered with one monolayer of hexagonal boron nitride. The work function difference of 1.8 eV of the two surfaces is reflected in the $\vec{k}_{\parallel}$ scaling with respect to the Ni(111) surface Brillouin zone that has been overlayed in both figures. Within the free-electron final state approximation, equivalent $\vec{k}$ vectors inside the solid are compared (see text; from Ref. [36]).

symmetry. This indicates an increased importance of the surface Ni layer: a two-dimensional (2D) hexagonal layer is associated with a sixfold 2D reciprocal lattice, whereas the 3D reciprocal lattice of the fcc structure, viewed along the [111] direction, has only threefold rotational symmetry. It should be mentioned that the states near the Fermi level remain essentially Ni states: the electronic structure of the boron nitride monolayer appears to be very similar to the van-der-Waals bonded bulk h-BN, with the σ band reaching a maximum binding energy of 5.2 eV at the Γ point and the π band reaching 4.5 eV at the K point of the layer Brillouin zone [37]. Dispersion plots show no distinct new bands of comparable spectral weight near ε_F such that one surmises that a band gap of ca. 5 eV persists also in the monolayer film. The conclusion is thus that the changes observed in the Fermi surface contour patterns (Fig. 9) reflect the response of the top layer Ni bands to the presence of the h-BN monolayer. To first approximation, most of the sixfold pattern can be recovered by umklapp scattering of the threefold symmetric Ni contours applying reciprocal lattice vectors of the 2D surface layer. Although the symmetry of the topmost Ni layer has not changed, the presence of the h-BN film seems to act like an atomic grating imposing thus the symmetry of its 2D lattice on the substrate bands of the adjacent layer [36]. Due to the small scattering cross sections of B and N atoms it is unlikely that this umklapp scattering is strong in the photoemission final state. Rather, weak interaction through hybridization of p_z orbitals of the film atoms with top-layer Ni states is likely to result in bonding states, located between the top Ni layer and the h-BN layer, that are essentially of 2D character. Due to their origin they couple strongly to the Ni bulk bands such that their Fermi surface contours can be derived from the original Ni contours. In fact they are probably not truly two-dimensional, they should look rather like surface resonances with a similar but broadened $k_{\perp}$-dispersion as the parent bulk states. Of course there will be slight hybridization-induced shifts — rather similar in character to surface core-level shifts — and it will be extremely interesting to

resolve these shifts in high-resolution dispersion plots. The data of Fig. 9b suggest that one sees the 2D contours of these bonding orbitals and the 3D contours from the underlying bands at the same time.

One expects that the modifications to the Ni bands in the close vicinity of an interface should have pronounced effects on the transport properties through such interfaces. Current theoretical models of giant magnetoresistance (GMR) and tunnelling magnetoresistance (TMR) have emphasized the role of the metallic or insulating spacer layer [40]. We now suspect that the very presence of the interface introduces new scattering processes also in the ferromagnetic layers, predominantly umklapp scattering involving 2D reciprocal lattice vectors, that are expected to influence the transmission through the interface.

4. Cobalt

4.1. Co(0001)

Like nickel, cobalt is a strong ferromagnet, i.e. the majority d band is completely filled. However, there are much less photoemission studies for cobalt, mainly for experimental reasons: Co metal goes through a structural phase transition near 700 K [41] that interferes with the usual preparation techniques for such transition metal surfaces that consist of repeated cycles of sputtering and annealing. On the close-packed Co(0001) surface an early synchrotron radiation photoemission study, using an energy resolution of the order of 100 meV, revealed dispersing features within the first 2 eV from the Fermi energy [42], and from an assignment of these bands in relation to a band structure calculation an estimate was given for the exchange splitting of 0.85 ± 0.2 eV of the d band features nearest to ε_F. Later studies using spin-polarized photoemission [43,44], although with reduced energy resolution, proved important in assigning the majority/minority character to the photoemission features unambiguously, and an increased exchange splitting of 1.15 ± 0.15 eV was found for that same band. These two studies were actually carried out on 20 monolayer (ML) thick films of Co on Cu(111) [43] and on W(110) [44]. A more recent higher resolution (40 meV), but spin-integrated photoemission experiment [45] on Co(0001) produced spectra in close agreement with those of Himpsel and Eastman [42], but failed to give well defined Fermi surface contours comparable in definition to those routinely observed on Ni surfaces, although the surface crystallinity was of a similar quality. It was argued that the stray magnetic fields above the intricate domain pattern of Co(0001), where the magnetization vector is perpendicular to the surface [46], is responsible for the very diffuse Fermi surface map.

Because of the much larger exchange splitting in Co, the assignment of majority and minority features is much more difficult than in Ni: can we expect to find pairs of bands with opposite spin character showing similar dispersion in some specific regions in $\vec{k}$-space that proved to be so important in the case of Ni? This question is intimately related to the question of how strong correlation effects act in Co to shift and broaden photoemission lines further away from the Fermi energy (see Section 4.3).

4.2. Co films on Cu(111)

The complications of perpendicular magnetization in the surface and stray magnetic fields above the surface can be avoided if thin films of Co are grown on a suitable substrate. Very recently, our group has studied the evolution of the Fermi surface of Co with film thickness for films grown on Cu(111) [47]. It was found that for films of less than 5 ML the Fermi surface maps change with thickness. Due to the complex morphology [48] and the presence of the underlying Cu signal for these very thin films, the contours are rather diffuse. They sharpen up with thickness, and for roughly 9–10 ML convergence is reached with a well-defined contour pattern (Fig. 10a). There are distinctly more features in this Fermi surface map than in the ones for Ni, which comes from the fact that there are two Co atoms per hcp unit cell and thus twice as many Fermi surface sheets in each Brillouin zone.

Again it is very useful to have bandstructure calculations available that can help identify the various bands crossing the Fermi level. In Fig. 10b the result of a calculation using the WIEN97 full-potential linearized augmented plane wave code [49] is shown, giving only the majority spin Fermi

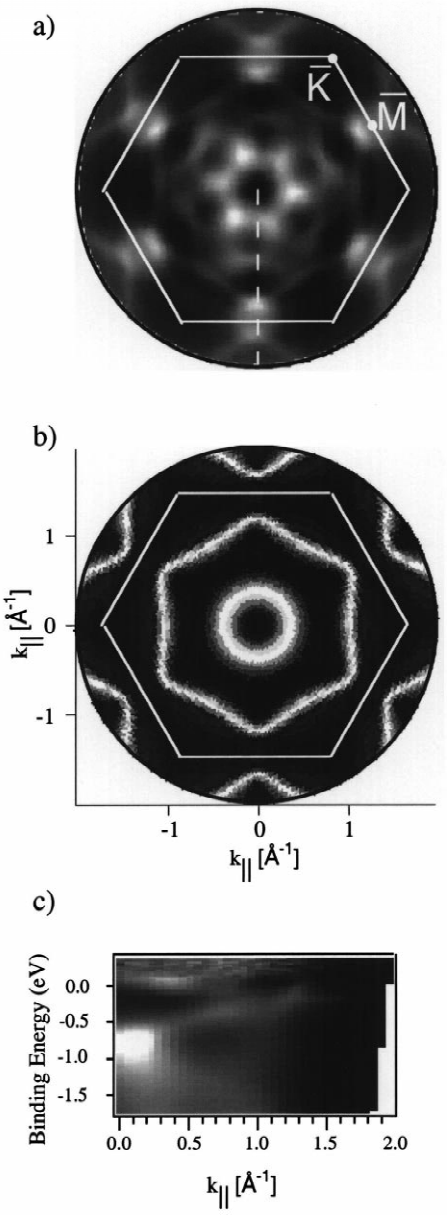

Fig. 10. (a) He Iα excited Fermi surface map ($h\nu = 21.21$ eV) from a 9 ML thick film of hexagonal close-packed Co on Cu(111). The surface Brillouin zone is overlayed (from Ref. [47]). (b) Full-potential linearized augmented plane wave (FLAPW) calculation for the majority spin Fermi surface map for hcp Co, for the same $\vec{k}$ space region below the (0001) surface as in (a). (c) Polar scan dispersion plot data measured along the dashed line of (a). Photoemission intensities have been normalized by the Fermi–Dirac distribution function and are given in a linear grey scale with maximum intensities in white.

surface sheets.[1] The two Fermi surface sheets inside the surface Brillouin zone, which coincides with the projection of the hcp bulk Brillouin zone, are readily seen. What is more important, they can also be seen in the measurement, although the smaller sheet appears somewhat sixfold modulated in the data. The larger sheet is also observed in the second Brillouin zones, both in the calculation and in the experiment. There is thus an excellent agreement for this sp-like majority Fermi surface map where manybody corrections are expected to be small. The minority Fermi surface is predominantly d-like in cobalt since the Fermi level has dropped deeper into the d-band than in nickel. Manybody corrections should thus be large for the minority bands near the Fermi level, and they appear to be important also on the Fermi surface (see below). Calculations for the minority spin Fermi surface map (not shown) using the same parameters as for the majority spin case do not give satisfactory results in terms of describing the experimental data. Nevertheless, these calculations have thus provided us again with a very useful guideline as to the spin character of the observed Fermi surface contours.

In Fig. 10c a polar dispersion plot including binding energies down to 1.8 eV is shown, measured along the $\bar{\Gamma}\bar{M}$ high symmetry azimuth. Except for one band that crosses the Fermi level at about 1.3 $Å^{-1}$ and which is associated with the larger one of the majority spin Fermi surface sheets, band dispersion seen in this figure is generally rather flat, much more so than in nickel, and the features appear rather diffuse. Again this impression may arise partly due to the presence of many closely-spaced bands, but it may also indicate that manybody effects are at least as important in the spectral function of cobalt as in nickel (see below). In any case there are no well defined pairs of bands that can readily be identified from their similar dispersion as being of the same orbital origin. It would thus be very interesting to study the evolution of these data with temperature.

[1] These calculations have been carried out by P. Aebi. In order to calculate the $\vec{k}$ vectors where the photoemission final states intersect the Fermi surface according to Eqs. (1)–(4), a work function Φ of 6.0 eV and an inner potential V_0 of 13.0 eV were chosen.

4.3. Correlation effects

In the ground state cobalt has more d holes than nickel. From Fig. 3 it is clear that this opens more scattering channels, and for comparable Coulomb integrals U the manybody corrections should thus be even more pronounced. A detailed analysis of spectral functions for Co using the 3BS formalism is currently underway [50]. Preliminary results indicate severe energy renormalization in the majority d band, essentially removing all d band spectral weight from the region below 1 eV binding energy but leading to a strong overlapping of d bands of both spin characters within the first eV binding energy below ε_F. This finding has, of course, strong implication for the interpretation of spin-resolved photoemission experiments and the reading of exchange splittings from such data, not to speak of spin-integrated experiments.

Minority spin Fermi surface sheets are strongly distorted from the single particle calculations, leading finally to a good agreement with the experimental data. Such distortions of the Fermi surface are consistent with the Luttinger theorem [27] as long as the volume is not changed. In a case like cobalt, where more than one d band crosses the Fermi level, even this condition may be relaxed and spectral weight may be redistributed between different bands by the manybody interactions.

5. Summary and outlook

The examples discussed in this paper have illustrated how photoemission data taken with relatively high energy and angular resolution have, for the cases of nickel and cobalt, brought new insight into the interplay between magnetism and manybody effects and how these phenomena are reflected in the spectra. In this context, the 3BS calculation for the spectral function [26] has been extremely useful and successful. Spin- and $\vec{k}$-dependent self-energy corrections to the spectral function produce strong shifts of measured bands away from their single-particle energy positions as obtained in bandstructure calculations. In the case of nickel the hierarchy of majority and minority spin bands is more or less preserved with an overall energy renormalization by a factor of the order of 2.5. In cobalt, the effects are significantly stronger, leading to a strong overlap of majority and minority bands close to the Fermi level [50].

For nickel, the ferromagnetic phase transition is very clearly reflected in the temperature behaviour of the bands near ε_F: both d bands and sp bands show a Stoner-like collapse of the exchange splitting. For cobalt — and also for iron — such temperature-dependent high-resolution photoemission experiments have not yet been performed. High Curie temperatures and structural phase transitions render these experiments very difficult, and one may have to resort to suitable thin film systems. The magnetic moments in these two metals are considerably larger and more stable, and the result of such experiments is by far not obvious.

The presence of adsorbates on nickel surfaces is found to affect the Ni d bands within the interfacial layer. In the context of strong correlations, where the manybody interactions are dominated by local on-site Coulomb integrals, it seems plausible to introduce the notion of a stratified, i.e. layered bandstructure. Angle-resolved valence photoemission probes several layers simultaneously and sees thus the superposition of interfacial and bulk bands, similar to the case of core level photoemission.

Especially in cobalt, where many bands crowd the region near ε_F it would be highly desirable to have spin-resolved measurements. The examples discussed in this paper make it clear that the energy and angular resolution must not be compromised. This represents thus a formidable experimental undertaking, considering the low detection efficiency of traditional spin detectors. A further difficulty arises in the case of Fermi surface mapping where the sample needs to be rotated freely about two independent axes. For a magnetized sample, which is required for spin-resolved experiments, the magnetization vector therefore covers as well a full hemisphere, and all components of the photoelectron spin have to be measured. A new spin-polarized photoemission experiment using a high-resolution hemispherical electron analyzer and two 60 keV Mott detectors [51], each capable of measuring spin-po-

larization along two perpendicular axes, is currently being constructed [52]. It will eventually run on a third generation synchrotron radiation source.

Acknowledgements

This paper reviews mainly work from the author's collaborations with T. Greber, T.J. Kreutz, P. Aebi, F. Manghi, E. Wetli, H.J. Neff and W. Auwärter. The author is grateful to M. Hengsberger for critically reading and improving the manuscript. This work was supported by the Swiss National Science Foundation.

References

[1] H. Capellmann, J. Magn. Magn. Mater. 28 (1982) 250.
[2] E.C. Stoner, Rep. Prog. Phys. 11 (1947) 43.
[3] E.P. Wohlfarth, Rev. Mod. Phys. 25 (1953) 211.
[4] J.F. Janak, Phys. Rev. B 16 (1977) 255.
[5] H.A. Mook, J.W. Lynn, R.M. Nicklow, Phys. Rev. Lett. 30 (1973) 556.
[6] S. Hüfner, Photoelectron Spectroscopy, Springer, Berlin, 1995.
[7] E. Kisker, C. Carbone, in: S.D. Kevan (Ed.), Angle-Resolved Photoemission, Elsevier, Amsterdam, 1992, Chapter 12.
[8] C.J. Maetz, U. Gerhardt, E. Dietz, A. Ziegler, R.J. Jelitto, Phys. Rev. Lett. 48 (1982) 1686.
[9] H. Hopster, R. Raue, G. Güntherodt, E. Kisker, R. Clauberg, M. Campagna, Phys. Rev. Lett. 51 (1983) 829.
[10] K.-P. Kämper, W. Schmitt, G. Güntherodt, Phys. Rev. B 42 (1990) 10696.
[11] P.A. Aebi, T.J. Kreutz, J. Osterwalder, R. Fasel, P. Schwaller, L. Schlapbach, Phys. Rev. Lett. 76 (1996) 1150.
[12] T. Greber, T.J. Kreutz, J. Osterwalder, Phys. Rev. Lett. 79 (1997) 4465.
[13] T.J. Kreutz, T. Greber, P. Aebi, J. Osterwalder, Phys. Rev. B 58 (1998) 1300.
[14] J.B. Pendry, Surf. Sci. 57 (1976) 679.
[15] M. Lindroos, A. Bansil, Phys. Rev. Lett. 77 (1996) 2985.
[16] A. Bansil, M. Lindroos, Phys. Rev. Lett. 83 (1999) 5154.
[17] C.N. Berglund, W.E. Spicer, Phys. Rev. A 136 (1964) 1030–1044.
[18] E. Bertel, M. Donath (Eds.), Electronic Surface States and Interface States on Metallic Systems, World Scientific, Singapore, 1995.
[19] P. Thiry, Ph.D. Thesis, Université de Paris-Sud, 1981.
[20] N.V. Smith, P. Thiry, Y. Petroff, Phys. Rev. B 47 (1993) 15476.
[21] T.J. Kreutz, P. Aebi, J. Osterwalder, Solid State Commun. 96 (1996) 339.
[22] P. Aebi, J. Osterwalder, R. Fasel, D. Naumovic, L. Schlapbach, Surf. Sci. 307–309 (1994) 917.
[23] J. Osterwalder, Surf. Rev. Lett. 4 (1997) 391.
[24] T. Greber, O. Raetzo, T.J. Kreutz, P. Schwaller, W. Deichmann, E. Wetli, J. Osterwalder, Rev. Sci. Instrum. 68 (1997) 4549.
[25] M. Donath, Surf. Sci. Rep. 20 (1994) 251, Comprehensive review.
[26] F. Manghi, V. Bellini, J. Osterwalder, T.J. Kreutz, P. Aebi, C. Arcangeli, Phys. Rev. B 59 (1999) R10409.
[27] J.M. Luttinger, Phys. Rev. 119 (1960) 1153.
[28] J.A. Hertz, D.M. Edwards, J. Phys. F: Metal Phys. 3 (1973) 2174.
[29] D.M. Edwards, J.A. Hertz, J. Phys. F: Metal Phys. 3 (1973) 2191.
[30] P. Aebi, F. Bourqui, Design of Heating Electronics, University of Fribourg, 1994.
[31] T. Valla, A.V. Fedorov, P.D. Johnson, B.O. Wells, S.L. Hulbert, Q. Li, G.D. Gu, N. Koshizuka, Science 285 (1999) 2110.
[32] F.J. Himpsel, D.E. Eastman, Phys. Rev. Lett. 41 (1978) 507.
[33] J. Kutzner, R. Paucksch, C. Jabs, H. Zacharias, J. Braun, Phys. Rev. B 56 (1997) 16003.
[34] B. Voigtländer, S. Lehwald, H. Ibach, Surf. Sci. 208 (1989) 113.
[35] E. Boschung, Th. Pillo, J. Hayoz, L. Patthey, P. Aebi, L. Schlapbach, Phys. Rev. B 58 (1998) R10210.
[36] T. Greber, W. Auwärter, J. Osterwalder, in: J.L. Morán-Lopéz (Ed.), The Physics of Low Dimensional Systems, Plenum, New York, 2001.
[37] A. Nagashima, N. Tejima, Y. Gamou, T. Kawai, C. Oshima, Phys. Rev. B 51 (1995) 4606.
[38] W. Auwärter, T.J. Kreutz, T. Greber, J. Osterwalder, Surf. Sci. 429 (1999) 229.
[39] Y. Gamou, M. Terai, A. Nagashima, C. Oshima, Sci. Rep. RITU A 44 (1997) 211.
[40] P. Bruno, Phys. Rev. B 52 (1995) 411.
[41] W. Betteridge, Prog. Mater. Sci. 24 (1979) 51.
[42] F.J. Himpsel, D.E. Eastman, Phys. Rev. B 21 (1980) 3207.
[43] U. Alkemper, C. Carbone, E. Vescovo, W. Eberhardt, O. Rader, W. Gudat, Phys. Rev. B 50 (1994) 17496.
[44] M. Getzlaff, J. Bansmann, J. Braun, G. Schönhense, J. Magn. Magn. Mater. 161 (1996) 70.
[45] E. Wetli, T.J. Kreutz, H. Schmid, T. Greber, J. Osterwalder, M. Hochstrasser, Surf. Sci. 402–404 (1998) 551.
[46] A. Hubert, R. Schäfer, Magnetic Domains, Springer, Berlin, 1998.
[47] J. Osterwalder, T. Greber, E. Wetli, J. Wider, H.J. Neff, Prog. Surf. Sci. 64 (2000) 65.
[48] Ch. Rath, J.E. Prieto, S. Müller, R. Miranda, K. Heinz, Phys. Rev. B 55 (1997) 10791.
[49] P. Blaha, K. Schwarz, J. Luitz, WIEN97, Vienna University of Technology, 1997, Improved and updated UNIX version of the original copyrighted WIEN code, published by P.

Blaha, K. Schwarz, P. Sorantin, S.B. Trickey, in Comput. Phys. Commun. 59 (1990) 399.
[50] F. Manghi, S. Monastra, C. Arcangeli et al., in preparation.
[51] V.N. Petrov, M. Landolt, M.S. Galaktionov, B.V. Yushenkov, Rev. Sci. Instrum. 68 (1997) 4385.
[52] M. Hoesch, T. Greber, M. Muntwiler, M. Hengsberger, J. Osterwalder, in preparation; see also http://www.physik.unizh.ch/groups/grouposterwalder/kspace/COPHEE.html